

## PDF hosted at the Radboud Repository of the Radboud University Nijmegen

The following full text is a preprint version which may differ from the publisher's version.

For additional information about this publication click this link.

<http://hdl.handle.net/2066/66876>

Please be advised that this information was generated on 2017-12-06 and may be subject to change.

# X-ray and optical observations of M55 and NGC 6366: evidence for primordial binaries

C. G. Bassa<sup>1,2</sup>, D. Pooley<sup>3</sup>, F. Verbunt<sup>1</sup>, L. Homer<sup>4\*</sup>, S. F. Anderson<sup>4</sup>, and W. H. G. Lewin<sup>5</sup>

<sup>1</sup> Astronomical Institute, Utrecht University, PO Box 80 000, 3508 TA Utrecht, The Netherlands

<sup>2</sup> Physics Department, McGill University, Montreal, QC H3A 2T8, Canada; e-mail: bassa@physics.mcgill.ca

<sup>3</sup> Astronomy Department, UC Berkeley, 601 Campbell Hall, Berkeley, CA 94720-3411, USA

<sup>4</sup> Department of Astronomy, University of Washington, Box 351580, Seattle, WA 98195, USA

<sup>5</sup> Kavli Institute for Astrophysics and Space Research, MIT, 77 Massachusetts Avenue, Cambridge, MA 02139, USA

Received / Accepted

## ABSTRACT

We present *Chandra X-ray Observatory* ACIS-S3 X-ray imaging observations and VLT/FORS2 and *Hubble Space Telescope* optical observations of two low-density Galactic globular clusters; NGC 6366 and M55. We detect 16 X-ray sources with 0.5–6.0 keV luminosities above  $L_X = 4 \times 10^{30}$  erg s<sup>-1</sup> within the half-mass radius of M55, of which 8 or 9 are expected to be background sources, and 5 within the half-mass radius of NGC 6366, of which 4 are expected to be background sources. Optical counterparts are identified for several X-ray sources in both clusters and from these we conclude that 3 of the X-ray sources in M55 and 2 or 3 of the X-ray sources in NGC 6366 are probably related to the cluster. Combining these results with those for other clusters, we find the best fit for a predicted number of X-ray sources in a globular cluster  $\mu_c = 1.2\Gamma + 1.1M_h$ , where  $\Gamma$  is the collision number and  $M_h$  is (half of) the cluster mass, both normalized to the values for the globular cluster M4. Some sources tentatively classified as magnetically active binaries are more luminous in X-rays than the upper limit of  $L_X \approx 0.001L_{\text{bol}}$  of such binaries in the solar neighbourhood. Comparison with *XMM* and *ROSAT* observations lead us to conclude that the brightest X-ray source in M55, a dwarf nova, becomes fainter in X-rays during the optical outburst, in accordance with other dwarf novae. The brightest X-ray source in NGC 6366 is a point source surrounded by a slightly offset extended source. The absence of galaxies and H $\alpha$  emission in our optical observations argues against a cluster of galaxies and against a planetary nebula, and we suggest that the source may be an old nova.

**Key words.** Globular clusters: individual (NGC 6366 and M55)

## 1. Introduction

All stars emit X-rays, but some emit more than others. Thanks to the *Chandra X-ray Observatory* the study of X-ray sources in globular clusters now includes sources down to luminosities of  $L_X \sim 10^{29-30}$  erg s<sup>-1</sup> in the 0.5–2.5 keV band. At these low luminosities, most sources are low-mass main-sequence stars that rotate rapidly, which in old stellar clusters is the case only when they have been spun up by tidal forces or by accretion in close binaries. At the high luminosity end,  $L_X \gtrsim 10^{32}$  erg s<sup>-1</sup>, most sources are low-mass X-ray binaries in which a neutron star accretes matter from a companion. At intermediate luminosities, most sources are cataclysmic variables (CVs). The clusters best studied at low X-ray luminosities are 47 Tuc (Heinke et al. 2005 and references therein) and M4 (Bassa et al., 2004).

Whereas the binaries of main-sequence stars are primordial, i.e. formed as binaries when the component stars formed, the low-mass X-ray binaries in globular clusters are thought to be formed in close stellar encounters that bring a previously single neutron star into a binary (see the review by Verbunt & Lewin 2006 and references therein). For cataclysmic variables both formation mechanisms, evolution from a primordial binary and capture of a previously single white dwarf in a close encounter, are viable, depending on the circumstances. The progenitor binary of a cataclysmic variable must be wide enough

to allow the more massive star to evolve into a fairly big giant, before it reaches its Roche lobe. Such wide binaries are destroyed (‘ionized’) in cores of globular clusters with densities  $\rho_0 \gtrsim 10^3 M_\odot \text{pc}^{-3}$  (Davies, 1997).

One would naively expect that all cataclysmic variables in these cores were formed in stellar encounters. However, it has been pointed out that cataclysmic variables that evolved in the low-density outskirts of globular clusters can sink towards the core at late times. Thus, the population of cataclysmic variables in dense cores can be a mixture of locally produced products of stellar encounters and recently arrived products of the evolution of primordial binaries (Ivanova et al. 2006; see also Hurley et al. 2007).

The number of stellar encounters in a globular cluster scales roughly with the collision number  $\Gamma \equiv \rho_0^2 r_c^3 / v$ , where  $\rho_0$  is the central density of the cluster,  $r_c$  the core radius, and  $v$  the central velocity dispersion. Through the virial theorem  $v \propto r_c \sqrt{\rho_0}$  and thus  $\Gamma \propto \rho_0^{1.5} r_c^2$  (Verbunt & Hut, 1987; Verbunt, 2003). The mass  $M$  of a cluster can be estimated from the total luminosity of a cluster, with use of a mass-to-light ratio appropriate for a cluster star population, and if necessary a bolometric correction. The number of X-ray sources in a globular cluster then may be expected to depend on the collision number (dynamical origin) and on the cluster mass (primordial origin); the form of the dependence depends on the type of binary, and therefore on the luminosity range that is studied.

\* Current address: Abbey College Cambridge, 7 Station Rd, Cambridge, CB1 2JB, United Kingdom

**Table 1.** Parameters of M55 and NGC 6366 used in this paper; core radius  $r_c$ , half-mass radius  $r_h$ , distance  $d$  and reddening  $E_{B-V} = A_V/3.1$  (taken from Harris 1996, version Feb 2003). The interstellar column  $N_H$  is computed from  $N_H = 1.79 \times 10^{21} \text{ cm}^{-2} A_V$ , see Predehl & Schmitt (1995).

Cluster	$r_c$ (')	$r_h$ (')	$d$ (kpc)	$E_{B-V}$	$N_H$ ( $\text{cm}^{-2}$ )
M55	2.83	2.89	5.3	0.08	$4.44 \times 10^{20}$
NGC 6366	1.83	2.63	3.6	0.71	$3.94 \times 10^{21}$

The brightest low-mass X-ray binaries, with  $L_X > 10^{35} \text{ erg s}^{-1}$ , are sufficiently rare that a cluster contains either none or one; in one case (M15) two. The probability that a cluster contains such a source scales with  $\Gamma$  (Verbunt & Hut, 1987). The fainter low-mass X-ray binaries, with  $10^{32} \lesssim L_X \lesssim 10^{35} \text{ erg s}^{-1}$ , are more numerous; the number of them in a cluster also scales with  $\Gamma$  (Heinke et al., 2003; Gendre et al., 2003; Pooley et al., 2003). These results appear to confirm the theoretical idea that neutron stars enter binaries in globular clusters via stellar encounters. Studies of globular clusters within other galaxies complicate the issue, because they indicate that the probability that a cluster contains a bright source depends on its metallicity, being higher for metal-rich clusters (e.g. Kundu et al. 2002), and furthermore scales with  $\rho_0^{1.5}$ , a shallower dependence on density than implied by a proportionality with  $\Gamma$  (Jordán et al., 2004).

The numbers of less luminous sources, mostly cataclysmic variables – hitherto only observed in globular clusters of our Milky Way – appear to have a more shallow dependence on central density  $N \propto \rho_0^\gamma$  with  $\gamma = 0.6 - 0.7$  (Heinke et al., 2003; Pooley et al., 2003). Heinke et al. (2006) find different values of  $\Gamma$  for bright and faint cataclysmic variables, with the boundary near  $10^{32} \text{ erg s}^{-1}$ . Finally, Kong et al. (2006) show that the number of sources (2-5 only!) in the low-density globular cluster NGC 288, a mixture of cataclysmic variables and binaries of main-sequence stars, scales with the mass of this cluster. Pooley & Hut (2006) successfully describe the number  $N$  of X-ray sources in globular clusters with an equation of the form  $N = aM + b\Gamma$ .

There are many uncertainties in the theoretical description of the formation of X-ray sources in globular clusters. We mention only the retained fraction of neutron stars; and the details of the spiral-in process which changes the wide orbit of the progenitor binary into the close orbit of a cataclysmic variable. To help untangle these uncertainties empirically we have observed a variety of globular clusters both in X-rays and in the optical. We have selected these clusters to span a wide range in central density, core radius, and mass. In this paper we discuss our observations of two clusters with relatively large core radii and low central densities: M55 and NGC 6366. Some parameters of both clusters are given in Tables 1 and 6.

Both clusters were observed with the *ROSAT* PSPC, which detected one source in the core of each cluster (Johnston et al., 1996). The position of the source in M55 was more accurately determined with a *ROSAT* HRI observation Verbunt (2001), and this source was later optically identified with a dwarf nova (Kaluzny et al., 2005). *XMM* detected five sources in the core of M55, one of them coincident with the *ROSAT* source (Webb et al., 2006).

## 2. X-ray observations

M55 was observed for 33.7 ks on 2004 May 11, and NGC 6366 was observed for 22.0 ks on 2002 July 5, both with the Advanced

CCD Imaging Spectrometer (ACIS) on the *Chandra* X-Ray Observatory with the telescope aim point on the back-side illuminated S3 chip. The data were taken in timed-exposure mode with the standard integration time of 3.24 s per frame and telemetered to the ground in faint mode.

Data reduction was performed using the CIAO 3.3 software provided by the *Chandra* X-ray Center<sup>1</sup>. The data were reprocessed using the CALDB 3.2.2 set of calibration files (gain maps, quantum efficiency, quantum efficiency uniformity, effective area) including a new bad pixel list made with the `acis_run_hotpix` tool. The reprocessing was done without including the pixel randomization that is added during standard processing. This omission slightly improves the point spread function. The data were filtered using the standard ASCA grades (0, 2, 3, 4, and 6) and excluding both bad pixels and software-flagged cosmic ray events. Intervals of strong background flaring were searched for, but none were found. The extraction of counts and spectra and the generation of response files was accomplished with ACIS Extract<sup>2</sup> (Broos et al. 2002, version 3.107), which calls many standard CIAO routines.

### 2.1. Source detection

The CIAO wavelet-based `wavdetect` tool was employed for source detection in both the 0.5–6.0 and 0.3–10.0 keV bands. We detected 29 sources on the entire S3 chip in the M55 observation and 12 in NGC 6366 observation. Of these sources, 15 (14) lie within the 2'89 half-mass radius (2'83 core radius) of M55, and 3 (3) lie within the 2'63 half-mass radius (1'83 core radius) of NGC 6366. We also searched part of the adjacent S4 CCD in the M55 observation since part of the half-mass region fell on this chip, but no sources were detected in this area. Furthermore, we examined adaptively-smoothed images (made from the CIAO `csmooth` tool) for significant point sources. In the M55 observation, we found two additional possible sources within the core radius. In the NGC 6366 observation, we also found two additional possible sources within the half-mass radius, one of which was within the core radius. Fig. 1 shows the location of the detected sources with respect to the cluster center and the core and half-mass radius.

All sources are consistent with being point sources, except for CX1 in NGC 6366, which appears to extend to a radius of about 20'' (Fig. 2). Visual inspection suggests the superposition of a point source and extended emission. To assess their spatial coincidence, we fit two gaussians plus a constant background to an image of the region. One gaussian approximates the point spread function, and the other is broader and describes the extended emission. Our best fit model gives source counts in rough agreement with the methods described in §2.2 and given in Table 3; according to the model, the point source has 17.4 net counts, and the extended source has 186.1 net counts. The two gaussians are offset from each other by  $2'4 \pm 1'1$ .

We will give two estimates of how many sources are related to each cluster. For the first estimate, we assume that all sources outside the half-mass radius are fore- or background sources,  $N_o = 14$  for M55 and 9 for NGC 6366. Taking the size of the S3 detector as  $8'4 \times 8'4 = 70.6 \text{ sq. arcmin}$ , the expected number of fore- or background sources within the half-mass radius  $r_h$ , expressed in arcmin, follows as  $N_e = N_o \pi r_h^2 / (70.6 - \pi r_h^2)$ . This gives  $N_e = 8.3$  for M55 and 4.0 for NGC 6366.

<sup>1</sup> <http://asc.harvard.edu>

<sup>2</sup> [http://www.astro.psu.edu/xray/docs/TARA/ae\\_users\\_guide.html](http://www.astro.psu.edu/xray/docs/TARA/ae_users_guide.html)

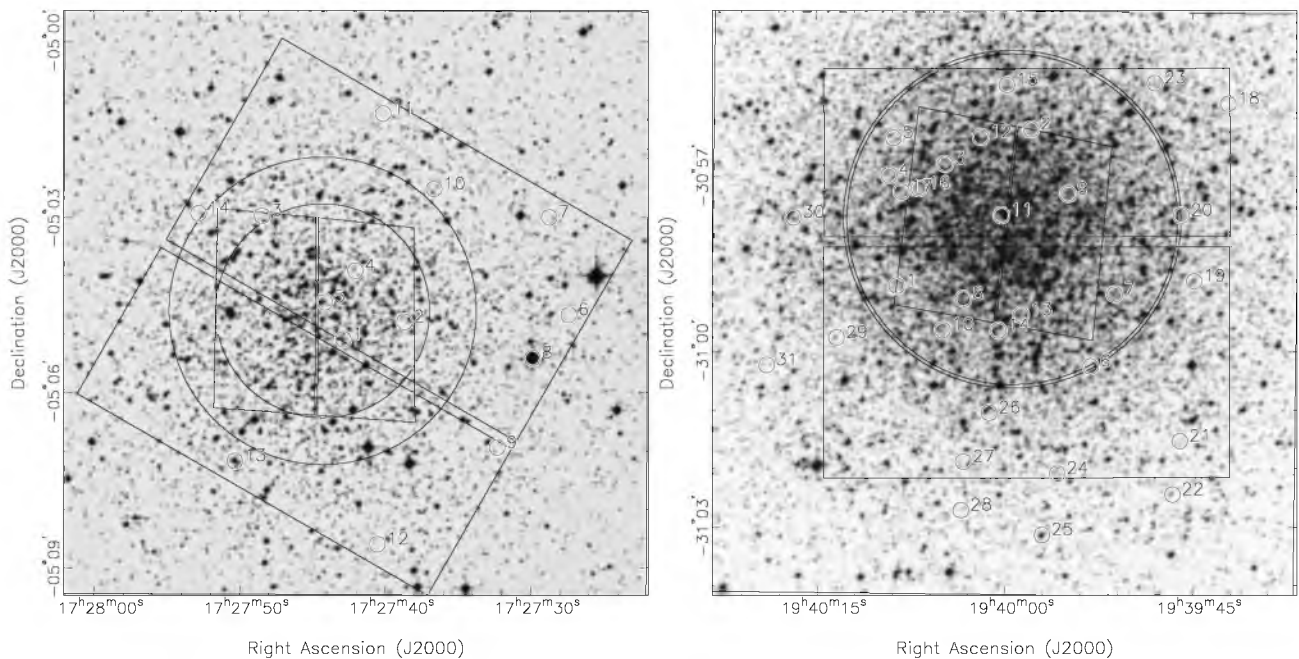


**Fig. 1.**  $10' \times 10'$  Digitized Sky Survey *R*-band images of M55 (*left*) and NGC 6366 (*right*). The positions of the *Chandra* X-ray sources are depicted with circles and numbered according to their CX designation (see Table 2 and 3). The two large rectangles on each image denotes the field-of-view of the two FORS2 chips, while the smaller slanted rectangles denote the field-of-view of the *Hubble Space Telescope* ACS/WFC chips.

The second estimate may be found from the  $\log N$ - $\log S$  relationships of Giacconi et al. (2001); at our detection limits, this leads to an expected number of background sources within the half-mass radius of 6–9 for M55 and 3–4 for NGC 6366. These numbers are wholly compatible with our first estimate. In M55 we detect 17 sources within the core, of which we estimate 8–11 cluster members. The probability to find 14 or more sources for expected 8.3 is about 4%; so it is likely that at least 4 sources are members. In the case of NGC 6366 we estimate that 1 of the 4 sources within the half-mass radius is a cluster member, but there is a sizable probability (37%) that all sources are foreground or background.

We repeat our first estimate for sources with  $L_X > 4 \times 10^{30} \text{ erg s}^{-1}$  [0.5–6.0 keV], the limit used in the Pooley et al. (2003) study. Above the corresponding flux limit of  $1.2 \times 10^{-15} \text{ erg s}^{-1} \text{ cm}^{-2}$  for M55, we detected 14 sources outside the half-mass radius of M55, and expect 8.3 sources unrelated to the cluster within the half-mass radius. 16 sources within the half-mass radius are observed above the flux limit. Above the flux limit for NGC 6366 of  $2.6 \times 10^{-15} \text{ erg s}^{-1} \text{ cm}^{-2}$ , we observe 9 sources outside the half-mass radius, which predicts 4.0 unrelated sources within the core, compared to the observed number of 5. The probability to observe 14 or more sources when 8.3 are expected is about 4%. Thus from the source numbers alone we have marginal evidence for sources above the luminosity limit used by Pooley et al. (2003) related to M55; and no evidence for such sources related to NGC 6366.

In Tables 2 and 3 we list the properties of the X-ray sources detected by *Chandra* in M55 and NGC 6366, respectively.

## 2.2. Count Rates

We extracted source counts in the following bands: 0.5–1.5 keV ( $X_{\text{soft}}$ ), 0.5–4.5 keV ( $X_{\text{med}}$ ), and 1.5–6.0 keV ( $X_{\text{hard}}$ ). The detected count rate was corrected for background, exposure vari-

ations, and foreground photoelectric absorption. We make these corrections in order to produce a X-ray color-magnitude diagram (CMD) that can be compared to the X-ray CMDs that have resulted from *Chandra* observations of other globular clusters. In addition, however, attention must be paid to differences in detector responses and, of course, exposure times and distances.

The background count rates in each band were estimated from source-free regions on the S3 chip outside the half-mass radii. The density of background counts in each band for the M55 observation is 0.0050 counts pixel $^{-1}$  in  $X_{\text{soft}}$ , 0.0103 counts pixel $^{-1}$  in  $X_{\text{med}}$ , and 0.0072 counts pixel $^{-1}$  in  $X_{\text{hard}}$ . For the NGC 6366 observation, the background densities are 0.0030 counts pixel $^{-1}$  in  $X_{\text{soft}}$ , 0.0063 counts pixel $^{-1}$  in  $X_{\text{med}}$ , and 0.0056 counts pixel $^{-1}$  in  $X_{\text{hard}}$ . The background count rates in the cores may be somewhat higher, but even factors of a few greater than this estimate have negligible effects on our analysis.

The exposure variations among sources were at the 15% level or less in both observations. To account for these variations in exposure, we applied multiplicative corrections based on the ratio of the average effective area of the detector at the location of a source in each of the three bands to that in the same band of the source which had the highest average exposure (CX11 in M55 and CX2 in NGC 6366). The individual effective area curves for the sources were made using the CIAO tool *mkarf*. The average effective area of the detector at the location of CX11 in M55 in each of the bands was 494 cm $^2$  ( $X_{\text{soft}}$ ), 449 cm $^2$  ( $X_{\text{med}}$ ), and 381 cm $^2$  ( $X_{\text{hard}}$ ); for CX2 in NGC 6366, the areas were 509 cm $^2$  ( $X_{\text{soft}}$ ), 447 cm $^2$  ( $X_{\text{med}}$ ), and 373 cm $^2$  ( $X_{\text{hard}}$ ).

While the previous corrections were relatively minor (at the few percent level or less), the correction for photoelectric absorption is appreciable for NGC 6366 (less so for M55). We investigated the effects of absorption by the column densities given in Table 1 on three characteristic spectra: a 3 keV thermal bremsstrahlung, a 0.3 keV blackbody plus power law with photon index of 2, and a power law with a photon index of 2.

**Table 2.** *Chandra* X-ray sources detected in our observation of M55. The positions of the X-ray sources have been corrected for the bore-sight correction of  $-0'.270$  in right ascension and  $+0'.080$  in declination. Positional uncertainties are given in parentheses and refer to the last quoted digit and are the centroiding uncertainties given by ACIS Extract. They do not include the uncertainties in the bore-sight correction ( $0'.044$  in right ascension and  $0'.045$  in declination). The X-ray bands are 0.5–1.5 keV ( $X_{\text{soft}}$ ), 0.5–4.5 keV ( $X_{\text{med}}$ ) and 1.5–6.0 keV ( $X_{\text{hard}}$ ). The first 17 sources are located within the half-mass radius of this cluster and are ordered on 0.5–6.0 keV countrate ( $X_{\text{soft}} + X_{\text{hard}}$ ). The remaining sources are located outside the half-mass radius and are ordered on right ascension. Some of the X-ray sources are also detected by *ROSAT* (Johnston et al., 1996; Verbunt, 2001) and *XMM* (Webb et al., 2006). These sources are denoted by R and X. CV1 is cataclysmic variable found by Kaluzny et al. (2005).

ID	R.A. (J2000)	Decl. (J2000)	Counts (Detected/Corrected)			$f_{\text{X}}$ (0.5–2.5 keV) (erg s <sup>-1</sup> cm <sup>-2</sup> )	$f_{\text{X}}$ (2.5–6.0 keV) (erg s <sup>-1</sup> cm <sup>-2</sup> )
			$X_{\text{soft}}$	$X_{\text{med}}$	$X_{\text{hard}}$		
CX1 (R9/X30/CV1)	19 <sup>h</sup> 40 <sup>m</sup> 08 <sup>s</sup> .593(3)	-30°58'52".08(4)	60/74.3	102/123.5	45/47.9	$1.2 \times 10^{-14}$	$1.4 \times 10^{-14}$
CX2 (X42)	19 <sup>h</sup> 39 <sup>m</sup> 57 <sup>s</sup> .877(3)	-30°56'11".67(4)	27/32.8	44/51.4	18/18.5	$5.0 \times 10^{-15}$	$5.8 \times 10^{-15}$
CX3 (X12)	19 <sup>h</sup> 40 <sup>m</sup> 04 <sup>s</sup> .720(3)	-30°56'47".09(4)	14/17.0	33/38.6	22/22.8	$3.4 \times 10^{-15}$	$7.9 \times 10^{-15}$
CX4 (X13)	19 <sup>h</sup> 40 <sup>m</sup> 09 <sup>s</sup> .192(5)	-30°56'58".54(7)	4/4.9	21/24.7	19/19.8	$1.9 \times 10^{-15}$	$7.2 \times 10^{-15}$
CX5	19 <sup>h</sup> 40 <sup>m</sup> 08 <sup>s</sup> .846(6)	-30°56'20".34(8)	10/11.8	15/17.5	7/7.5	$1.9 \times 10^{-15}$	$2.1 \times 10^{-15}$
CX6	19 <sup>h</sup> 39 <sup>m</sup> 53 <sup>s</sup> .108(11)	-31°00'14".99(15)	5/6.0	12/13.8	8/8.2	$1.3 \times 10^{-15}$	$2.3 \times 10^{-15}$
CX7	19 <sup>h</sup> 39 <sup>m</sup> 51 <sup>s</sup> .190(9)	-30°59'01".01(11)	10/11.8	13/14.7	3/3.1	$1.7 \times 10^{-15}$	$1.1 \times 10^{-15}$
CX8	19 <sup>h</sup> 40 <sup>m</sup> 03 <sup>s</sup> .279(8)	-30°59'05".61(11)	5/6.2	10/12.1	6/6.5	$1.2 \times 10^{-15}$	$1.6 \times 10^{-15}$
CX9	19 <sup>h</sup> 39 <sup>m</sup> 54 <sup>s</sup> .920(7)	-30°57'18".01(8)	0/0.0	8/9.3	10/10.2	$6.1 \times 10^{-16}$	$3.6 \times 10^{-15}$
CX10	19 <sup>h</sup> 40 <sup>m</sup> 04 <sup>s</sup> .932(11)	-30°59'37".68(15)	3/3.7	9/10.9	6/6.5	$9.2 \times 10^{-16}$	$1.7 \times 10^{-15}$
CX11	19 <sup>h</sup> 40 <sup>m</sup> 00 <sup>s</sup> .235(8)	-30°57'39".85(10)	3/3.3	7/7.3	4/3.6	$8.1 \times 10^{-16}$	$6.4 \times 10^{-16}$
CX12	19 <sup>h</sup> 40 <sup>m</sup> 01 <sup>s</sup> .887(8)	-30°56'19".48(10)	2/2.4	5/5.9	4/4.2	$5.8 \times 10^{-16}$	$1.2 \times 10^{-15}$
CX13	19 <sup>h</sup> 39 <sup>m</sup> 58 <sup>s</sup> .668(12)	-30°59'22".01(16)	0/0.0	5/6.3	6/7.0	$4.8 \times 10^{-16}$	$2.4 \times 10^{-15}$
CX14	19 <sup>h</sup> 40 <sup>m</sup> 00 <sup>s</sup> .479(14)	-30°59'38".08(18)	0/0.0	5/5.4	5/5.1	$4.3 \times 10^{-16}$	$1.4 \times 10^{-15}$
CX15	19 <sup>h</sup> 39 <sup>m</sup> 59 <sup>s</sup> .793(10)	-30°55'26".12(13)	4/5.4	5/6.3	1/0.8	$6.4 \times 10^{-16}$	$5.8 \times 10^{-16}$
CX16	19 <sup>h</sup> 40 <sup>m</sup> 06 <sup>s</sup> .829(10)	-30°57'12".29(13)	5/6.4	5/5.9	0/0.0	$7.6 \times 10^{-16}$	$2.0 \times 10^{-17}$
CX17	19 <sup>h</sup> 40 <sup>m</sup> 08 <sup>s</sup> .214(12)	-30°57'15".47(15)	3/3.7	4/4.6	1/0.8	$5.7 \times 10^{-16}$	$6.9 \times 10^{-16}$
CX18 (R6/X9)	19 <sup>h</sup> 39 <sup>m</sup> 42 <sup>s</sup> .130(4)	-30°55'45".48(5)	71/101.4	137/170.8	72/75.8	$1.8 \times 10^{-14}$	$2.0 \times 10^{-14}$
CX19	19 <sup>h</sup> 39 <sup>m</sup> 44 <sup>s</sup> .842(13)	-30°58'47".54(17)	5/6.4	11/12.8	6/6.0	$1.2 \times 10^{-15}$	$2.0 \times 10^{-15}$
CX20 (X14)	19 <sup>h</sup> 39 <sup>m</sup> 45 <sup>s</sup> .876(4)	-30°57'40".03(4)	29/38.5	92/112.6	78/82.9	$9.7 \times 10^{-15}$	$2.9 \times 10^{-14}$
CX21	19 <sup>h</sup> 39 <sup>m</sup> 45 <sup>s</sup> .989(19)	-31°01'31".65(25)	4/5.2	14/15.2	13/12.0	$1.5 \times 10^{-15}$	$4.7 \times 10^{-15}$
CX22 (X19)	19 <sup>h</sup> 39 <sup>m</sup> 46 <sup>s</sup> .573(12)	-31°02'26".47(15)	33/44.2	65/77.3	34/33.9	$8.1 \times 10^{-15}$	$1.2 \times 10^{-14}$
CX23	19 <sup>h</sup> 39 <sup>m</sup> 47 <sup>s</sup> .994(11)	-30°55'24".12(14)	8/23.8	11/28.6	3/6.5	$3.5 \times 10^{-15}$	$1.2 \times 10^{-15}$
CX24 (R13/X17)	19 <sup>h</sup> 39 <sup>m</sup> 55 <sup>s</sup> .778(4)	-31°02'04".98(5)	207/264.9	304/368.1	106/112.5	$3.9 \times 10^{-14}$	$2.6 \times 10^{-14}$
CX25 (X21)	19 <sup>h</sup> 39 <sup>m</sup> 57 <sup>s</sup> .005(15)	-31°03'07".82(19)	45/56.2	48/56.0	3/2.0	$7.1 \times 10^{-15}$	$4.8 \times 10^{-16}$
CX26	19 <sup>h</sup> 40 <sup>m</sup> 01 <sup>s</sup> .219(18)	-31°01'02".60(24)	0/0.0	3/3.0	7/7.1	$6.9 \times 10^{-16}$	$3.9 \times 10^{-15}$
CX27	19 <sup>h</sup> 40 <sup>m</sup> 03 <sup>s</sup> .284(24)	-31°01'52".73(31)	0/0.0	8/9.4	9/8.8	$6.4 \times 10^{-16}$	$3.1 \times 10^{-15}$
CX28 (X20)	19 <sup>h</sup> 40 <sup>m</sup> 03 <sup>s</sup> .475(14)	-31°02'42".40(18)	25/30.0	37/42.7	13/12.6	$4.7 \times 10^{-15}$	$4.2 \times 10^{-15}$
CX29 (X45)	19 <sup>h</sup> 40 <sup>m</sup> 13 <sup>s</sup> .402(15)	-30°59'45".22(19)	9/11.0	11/13.1	2/2.2	$1.6 \times 10^{-15}$	$7.7 \times 10^{-16}$
CX30	19 <sup>h</sup> 40 <sup>m</sup> 16 <sup>s</sup> .842(13)	-30°57'41".89(17)	4/5.5	10/12.3	6/6.0	$1.0 \times 10^{-15}$	$3.0 \times 10^{-15}$
CX31	19 <sup>h</sup> 40 <sup>m</sup> 18 <sup>s</sup> .981(20)	-31°00'13".35(26)	2/2.2	12/14.5	12/12.1	$1.3 \times 10^{-15}$	$5.0 \times 10^{-15}$

The effects were most prominent in the  $X_{\text{soft}}$  band. Averaging the results of each spectrum in each band, we use the following correction factors for NGC 6366: 3.72 ( $X_{\text{soft}}$ ), 2.47 ( $X_{\text{med}}$ ), and 1.17 ( $X_{\text{hard}}$ ). For M55, the factors are 1.21 ( $X_{\text{soft}}$ ), 1.16 ( $X_{\text{med}}$ ), and 1.02 ( $X_{\text{hard}}$ ). Table 2 and 3 list both the observed and fully corrected counts in each band. The effect of the absorption correction on the X-ray CMD (Fig. 3) is a uniform shift of the NGC 6366 sources by 0.39 units on the left axis and 0.50 units on the bottom axis and a uniform shift of the M55 sources by 0.06 units on the left axis and 0.07 units on the bottom axis. The bottom and left axes give the X-ray color and magnitude without this shift (they do, however, include the small corrections for background subtraction and exposure variations).

### 2.3. Spectral Fitting

We fit all sources with absorbed power-law spectral models in *Sherpa* (Freeman et al., 2001) using Cash (1979) statistics. We fixed the column density to the value given in Table 1, with only the power law photon index and normalization allowed to vary.

From the best fit spectra, we calculated the unabsorbed fluxes, given in Tables 2, 3.

For the point source NGC 6366 CX1a, the fluxes quoted in Table 3 are from a fit of an absorbed power law to the unbinned spectrum, for which we use Cash statistics, and fix the absorption to that of NGC 6366. This gave a power-law with photon index  $3.5 \pm 0.6$ . For the extended source NGC 6366 CX1b we extracted the spectrum from within a  $40''$  radius centered on CX1a. We subtracted the spectrum of the point source CX1a, and used a nearby, source-free, region with  $1'$  radius to estimate the background. This gave a bremsstrahlung temperature of the extended component of  $kT = 2.0^{+1.3}_{-0.7}$  keV, and unabsorbed fluxes as listed in Table 3.

### 3. Optical observations

Optical observations of M55 and NGC 6366 were obtained with the FORS2 instrument at the Unit Telescope 1 (UT1) of the ESO VLT in April and May 2005. Both globular clusters were observed in three filters, *B*, *R* and *H $\alpha$* , with exposure times chosen to maximize the dynamic range. Table 4 provides a condensed

**Table 3.** *Chandra* X-ray sources detected in our observation of NGC 6366. The celestial positions of the X-ray sources have been corrected for the bore-sight correction of  $+0'030$  in right ascension and  $-0'256$  in declination. Positional uncertainties are given in parenthesis and refer to the last quoted digit and are the centroiding uncertainties given by ACIS Extract. They do not include the uncertainties in the bore-sight correction ( $0'091$  in right ascension and  $0'082$  in declination). The X-ray bands are as defined in Table 2. The first 5 sources are located within the half-mass radius of this cluster and are ordered on 0.5–6.0 keV countrate ( $X_{\text{soft}} + X_{\text{hard}}$ ). The remaining sources are located outside the half-mass radius and are ordered on right ascension. CX1 was also detected by *ROSAT* (Johnston et al., 1996; Verbunt, 2001).

ID	R.A. (J2000)	Decl. (J2000)	Counts (Detected/Corrected)			$f_X$ (0.5–2.5 keV) ( $\text{erg s}^{-1} \text{cm}^{-2}$ )	$f_X$ (2.5–6.0 keV) ( $\text{erg s}^{-1} \text{cm}^{-2}$ )
			$X_{\text{soft}}$	$X_{\text{med}}$	$X_{\text{hard}}$		
CX1a	17 <sup>h</sup> 27 <sup>m</sup> 42 <sup>s</sup> 892(7)	-05°05'05".28(11)	10/33.2	15/32.1	5/4.8	$8.5 \times 10^{-15}$	$7.0 \times 10^{-16}$
CX1b (R4)	17 <sup>h</sup> 27 <sup>m</sup> 42 <sup>s</sup> 78(7)	-05°05'04".7(1.1)	87/190.0	185/280.9	111/79.2	$4.6 \times 10^{-14}$	$4.9 \times 10^{-14}$
CX2	17 <sup>h</sup> 27 <sup>m</sup> 38 <sup>s</sup> 682(7)	-05°04'47".63(11)	2/7.5	6/15.0	5/5.9	$1.4 \times 10^{-15}$	$2.8 \times 10^{-15}$
CX3	17 <sup>h</sup> 27 <sup>m</sup> 48 <sup>s</sup> 470(19)	-05°02'58".69(28)	2/7.7	5/11.5	3/2.8	$1.3 \times 10^{-15}$	$2.4 \times 10^{-15}$
CX4	17 <sup>h</sup> 27 <sup>m</sup> 42 <sup>s</sup> 044(12)	-05°03'55".12(18)	0/0.0	4/10.8	4/5.2	$5.5 \times 10^{-16}$	$3.1 \times 10^{-15}$
CX5	17 <sup>h</sup> 27 <sup>m</sup> 44 <sup>s</sup> 137(12)	-05°04'27".20(17)	3/12.1	5/13.4	2/2.6	$2.7 \times 10^{-15}$	$3.6 \times 10^{-16}$
CX6	17 <sup>h</sup> 27 <sup>m</sup> 27 <sup>s</sup> 384(8)	-05°04'40".42(12)	5/20.1	15/38.6	10/12.0	$4.6 \times 10^{-15}$	$3.7 \times 10^{-15}$
CX7	17 <sup>h</sup> 27 <sup>m</sup> 28 <sup>s</sup> 726(16)	-05°03'00".34(24)	2/7.7	6/15.0	6/7.2	$1.7 \times 10^{-15}$	$3.6 \times 10^{-15}$
CX8	17 <sup>h</sup> 27 <sup>m</sup> 29 <sup>s</sup> 883(6)	-05°05'24".56(8)	15/54.7	17/40.9	2/2.1	$1.5 \times 10^{-14}$	$1.7 \times 10^{-16}$
CX9	17 <sup>h</sup> 27 <sup>m</sup> 32 <sup>s</sup> 307(7)	-05°06'56".56(10)	2/6.7	8/19.9	6/7.1	$2.2 \times 10^{-15}$	$2.2 \times 10^{-15}$
CX10	17 <sup>h</sup> 27 <sup>m</sup> 36 <sup>s</sup> 643(17)	-05°02'31".24(26)	1/4.0	2/5.4	2/2.6	$1.8 \times 10^{-15}$	$5.1 \times 10^{-15}$
CX11	17 <sup>h</sup> 27 <sup>m</sup> 40 <sup>s</sup> 138(7)	-05°01'13".76(10)	36/141.8	80/207.4	45/55.2	$2.9 \times 10^{-14}$	$1.6 \times 10^{-14}$
CX12	17 <sup>h</sup> 27 <sup>m</sup> 40 <sup>s</sup> 533(9)	-05°08'35".70(14)	0/0.0	5/12.7	6/6.9	$7.0 \times 10^{-16}$	$5.2 \times 10^{-15}$
CX13	17 <sup>h</sup> 27 <sup>m</sup> 50 <sup>s</sup> 335(14)	-05°07'10".27(21)	4/15.1	6/14.7	2/2.1	$5.3 \times 10^{-15}$	$8.3 \times 10^{-17}$
CX14	17 <sup>h</sup> 27 <sup>m</sup> 52 <sup>s</sup> 830(11)	-05°02'56".05(16)	16/62.0	29/71.4	13/14.6	$1.0 \times 10^{-14}$	$5.5 \times 10^{-15}$

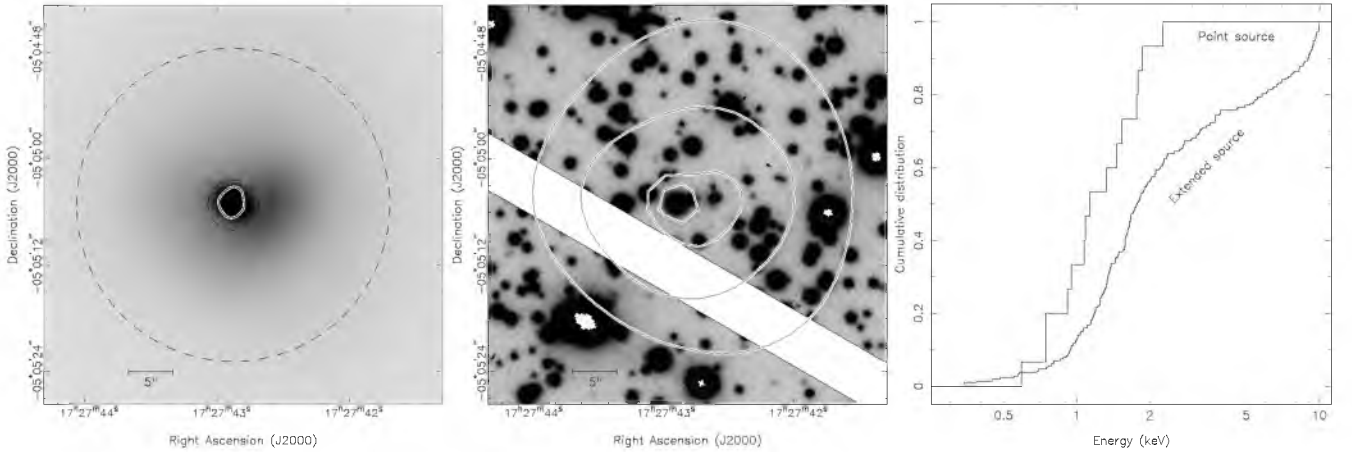


**Fig. 2.** (*left panel*) The adaptively smoothed brightness distribution of NGC 6366 CX1 shows a point source and an extended source. The solid contour contains 90% of the flux in the *Chandra* point spread function (at the detector location of the source); the dashed contours indicate the extraction region for the counts of the extended source. (*middle panel*) Contours from the adaptively smoothed brightness distribution of CX1 overlaid on the 15 minute  $H\alpha$  images. The white diagonal strip is due to the gap between the FORS2 chips, see Fig. 1. There is no evidence for any extended  $H\alpha$  emission. (*right panel*) The cumulative energy distributions of the point source (large-stepped distribution) and the extended source. A Kolmogorov Smirnov test gives a probability of 1% that both energy distributions are the same, and we conclude that the extended source is harder.

log of the observations. FORS2 is a mosaic of two  $2k \times 4k$  chips with a pixel scale of  $0'.126 \text{ pix}^{-1}$ . For the majority of the observations, we used  $2 \times 2$  on-chip binning, providing a pixel scale of  $0'.252 \text{ pix}^{-1}$ , except when the seeing was below  $0'.6$ , when no binning was applied.

The images were reduced using the Munich Image Data Analysis System (MIDAS). All images were bias-subtracted and flatfielded using twilight flats. Next, we grouped the images sharing the same combination of chip, filter and exposure time. The images in each group were aligned using integer pixel offsets and co-added to remove cosmic rays and increase the signal-to-noise. Hence, for each cluster we obtained 18 separate stacked images, 9 for each chip.

Both M55 and NGC 6366 are part of a survey of globular clusters with ACS/WFC on board the *Hubble Space Telescope*. M55 was observed for 284 s in a V-band filter (F606W) and 384 s in an I-band filter (F814W). For NGC 6366 the exposure times with 570 s in both F606W and F814W. Compared to FORS2, ACS/WFC has a smaller field-of-view (about  $3'4 \times 3'4$ ) and contains only a few of the X-ray sources. For M55, CX2, CX3, CX8, CX9, CX11, CX12, CX13 and CX16 are coincident with the  $202'' \times 202''$  field of view, while for NGC 6366 CX1 through CX5 are coincident.

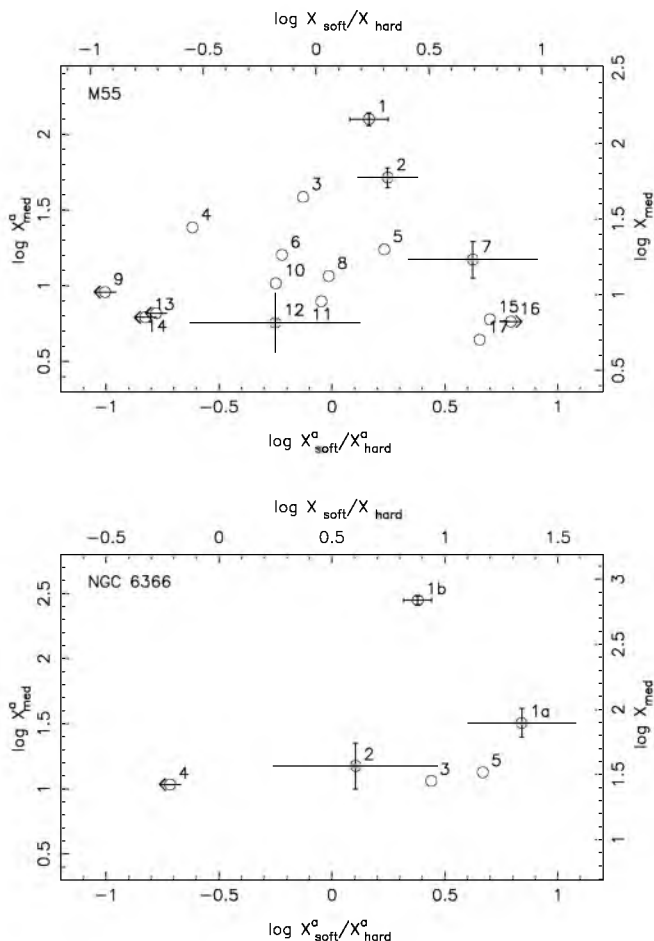


**Fig. 3.** X-ray color-magnitude diagram for the X-ray sources detected in the half-mass radius of M55 (*top panel*) and NGC 6366 (*bottom panel*). The X-ray color is defined as the logarithm of the ratio of  $X_{\text{soft}}$  (0.5–1.5 keV) counts to  $X_{\text{hard}}$  (1.5–6.0 keV) counts. The X-ray magnitude is the logarithm of  $X_{\text{med}}$  (0.5–4.5 keV) counts. The bottom and left axes provide the observed absorbed color and magnitude scales (<sup>a</sup>).

### 3.1. Photometry

We used DAOPHOT II, running inside MIDAS, for the photometry of the stacked FORS2 images. We followed the recommendations of Stetson (1987) and obtained instrumental magnitudes using point-spread-function (PSF) fitting. The PSF for each stacked image was determined in an iterative manner. First, we used an analytic PSF to remove stars in the proximity of those stars used to determine the PSF. This subsequently improved the PSF for the next iteration. We found that allowing the final PSF to quadratically depend on the position on the chip decreased the fitting residuals. We used the final PSF to determine instrumental magnitudes of all stars above a  $5\sigma$  detection threshold. The resulting star-subtracted image was then searched for objects that were missed in the first iteration. These stars were added to the star list after which the PSF-fitting process was repeated.

In order to match the stars found on the separate stacked images, we employed the following method. First, we determined approximate coordinate transformations between the separate images taken with the same chip of each cluster to create a single list containing all stars. Next, we removed multiple entries of the same star from the list by removing stars located with 3 pixels of another star. The resulting master star list was

**Table 4.** A log of the optical observations. Here,  $\sigma$  denotes the seeing and  $\sec z$  the airmass.

Date & Time (UT)	Exp. ( $B$ , $R$ , $H\alpha$ )	$\sigma$ (")	$\sec z$
NGC 6366			
April 8 07:40–09:20	4× (5 m, 2 m, 15 m)	0.6–0.7	1.06–1.13
April 9 07:22–08:10	2× (5 m, 2 m, 15 m)	0.7–1.0	1.09–1.16
08:13–08:24	6× (3 s, 1 s, 9 s)	0.7–1.1	1.07–1.08
08:25–08:47	6× (30 s, 12 s, 90 s)	0.6–0.8	1.06–1.07
M55			
April 10 08:01–09:51	4× (5 m, 2 m, 15 m) <sup>a</sup>	0.4–0.6	1.06–1.33
May 6 06:37–06:49	5× (3 s, 1 s, 9 s)	0.6–0.8	1.22–1.26
06:50–07:05	4× (30 s, 12 s, 90 s)	0.7–0.9	1.18–1.22
May 12 07:07–08:00	2× (5 m, 2 m, 15 m) <sup>a</sup>	0.4–0.5	1.04–1.11

<sup>a</sup> These observations were obtained with  $1 \times 1$  binning.

then matched against the star lists for each of the separate images, again using the approximate coordinate transformations. We determined improved, 6 parameter, coordinate transformations from the matched master list and repeated the process of creating a master list and matching stars.

Finally, the instrumental magnitudes for the separate chips were calibrated against photometric standards in the Mark A (for M55) and the Rubin 152 fields (for NGC 6366), using calibrated magnitudes from Stetson (2000) and fitting for zero-point and colour coefficients. Extinction coefficients in  $B$  and  $R$  were taken from the FORS2 webpage. The final rms residuals of the calibrations were 0.03 mag in  $B$  and 0.04 mag in  $R$  for the calibration of the NGC 6366 observations and 0.06 mag in  $B$  and 0.04 mag in  $R$  for the M55 observations. The  $H\alpha$  magnitudes were calibrated by adopting  $R - H\alpha = 0$  for the bulk of the stars. Fig. 4 shows colour-magnitude diagrams (CMDs) for both globular clusters.

For both clusters, we estimate  $5\sigma$  limiting magnitudes of  $B = 26.2$  and  $H\alpha = 24.8$ . The  $R$ -band magnitudes are limited through the calibration, which relies on the instrumental  $B - R$  colors and which is not available if a star is not detected in the  $B$ -band images. Hence, the  $R$ -band limit depends on the  $B - R$  color through  $R = 26.2 - (B - R)$ .

For the ACS/WFC observations we used the photometry presented in Anderson et al. (2008), who use highly specialized methods to determine accurate photometry of ACS/WFC images. For our purposes, we have used the photometry that was transferred from the ACS/WFC filters into ground-based  $V$  and  $I$ -band magnitudes. Fig. 5 shows the CMDs for both globular clusters.

### 3.2. Astrometry

We aim to tie the stacked  $R$ -band images for each globular cluster and each CCD to the International Celestial Reference System (ICRS), to astrometrically calibrate our photometric catalog and to allow for a comparison between the X-ray and optical frames. For each globular cluster and each CCD, we calibrated the stacked 1 s  $R$ -band images against UCAC2 astrometric standards (Zacharias et al., 2004). Even though the stellar density in the cores of these globular clusters is higher than a typical stellar field, our astrometry did not suffer from severe blending of stars, and for each image only 3 to 6 stars of the 40 to 80 that overlapped with each image were rejected. Fitting for zero-point position, scale and position angle, we obtained astrometric solutions for each image that had root-mean-square (rms) residuals of  $0''.04$  to  $0''.07$  in right ascension and declination. These solutions were transferred to the deeper  $R$ -band images using the cal-



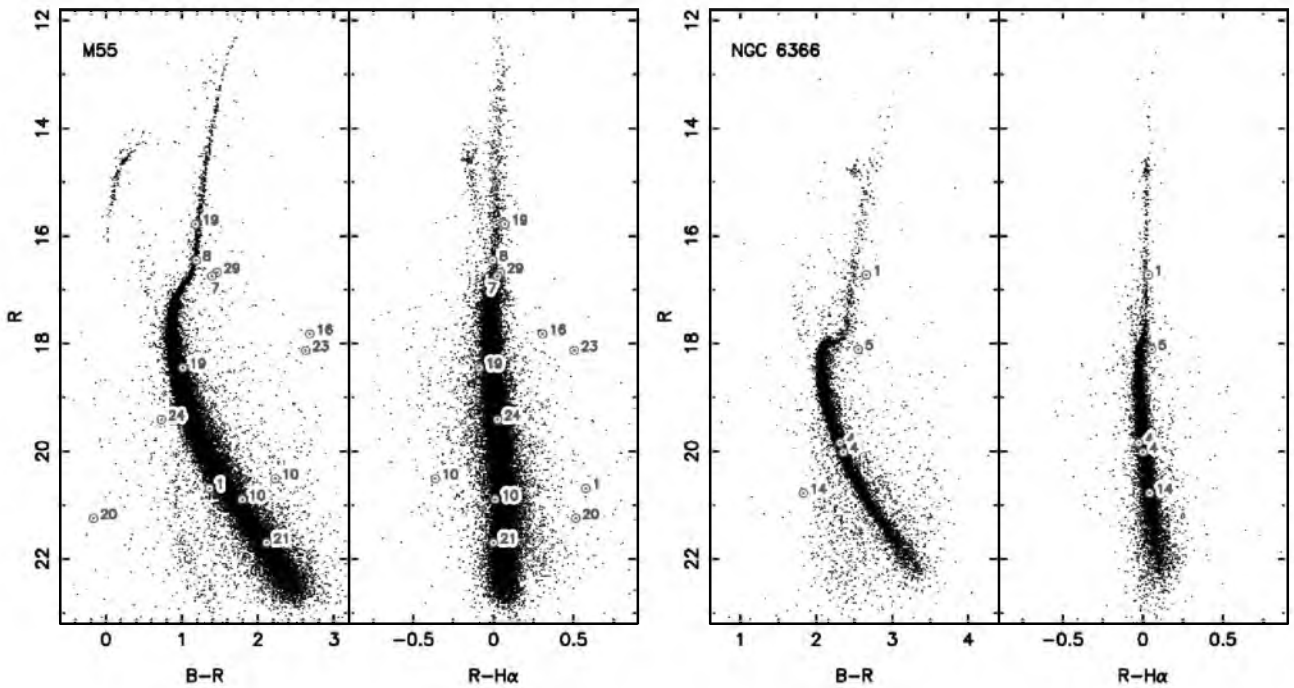


**Fig. 4.** Optical color-magnitude diagrams for M55 and NGC 6366 constructed from the FORS2 data. Candidate optical counterparts to the *Chandra* X-ray sources are indicated and numbered.

ibrated positions of stars on the 1 s images and used to calibrate the photometric catalog for each globular cluster. Typically, each solution used some 1300 to 1900 stars, resulting in rms residuals of  $0''.01$  to  $0''.03$ .

The drizzled ACS/WFC F606W images were calibrated against the FORS2 observations. Due to the large number of stars (500 to 700) coincident between the FORS2 and ACS/WFC images, the astrometric calibration has rms uncertainties of less than  $0''.02$  in right ascension and declination.

To place the *Chandra* frame onto the ICRS we use identifications based on the *Chandra* X-ray sources alone. We identify M55 CX1 with the dwarf nova CV1 discovered by Kaluzny et al. (2005). From the position of the optical counterpart, using the astrometry presented above, we determine a *Chandra* bore-sight correction of  $\Delta\alpha = -0''.270 \pm 0''.044$  and  $\Delta\delta = +0''.080 \pm 0''.045$ . For NGC 6366, we find that CXOJ172729.9–050524 coincides with the bright star ( $V = 10.7$ ) BD–04°4280 (PPM 706759; Röser & Bastian 1988). This star is saturated in our observations, but an accurate position is provided in the 2nd version of the USNO CCD Astrograph Catalog (UCAC2; Zacharias et al. 2004). The bore-sight correction is  $\Delta\alpha = +0''.030 \pm 0''.091$  and  $\Delta\delta = -0''.256 \pm 0''.082$ . These offsets put the X-ray positions onto the International Celestial Reference System (ICRS). We note that the uncertainty in both corrections is dominated by the uncertainty in the X-ray position. Both corrections, however, are within the  $0''.6$  (90% confidence) accuracy in the pointing of *Chandra* (Aldcroft et al., 2000).

With the optical and X-ray astrometry, the final uncertainty on the position of a X-ray source is the quadratic sum of the centroiding uncertainty of the X-ray source (those tabulated in Table 2 and 3), the uncertainty in the X-ray bore-sight correction, and the uncertainty in the astrometry of the *R*-band image. The resulting  $1\sigma$  uncertainties on the X-ray positions range between  $0''.1$  for the brightest X-ray source to  $0''.7$  for the fainter sources. In order to identify the optical counterparts to the X-ray sources, we treat every star inside the 99% confidence error circle as a

potential counterpart. These stars are indicated in the CMDs in Fig. 4 and Fig. 5 and finding charts are provided in Fig. 6.

#### 4. Source classification

As in our previous papers (Pooley et al., 2002; Bassa et al., 2004; Kong et al., 2006), we first use our astrometry to identify stars within the, in this case, 99% confidence circles as possible optical counterparts to the X-ray sources. We then check whether these stars have unusual photometric properties as expected for candidate counterparts. Finally we combine the optical photometry of the candidate counterparts, the X-ray properties of the X-ray sources and the combined  $f_X/f_{\text{opt}}$  to classify the probable counterparts. These steps are illustrated with Figures 6, 4, 3 and 7, respectively. For the latter figure, we estimate the visual magnitude as  $V = (B + R)/2$  where no *V*-band magnitudes are available. The photometry and the offset between the *Chandra* and optical positions are given for selected optical counterparts in Table 5.

##### 4.1. M55

Starting with M55, we note that the 99% error circles in Fig. 6 include relatively bright stars for CX1, CX7, CX8, CX10, and CX16. The other circles contain no significant stars, or stars that we consider too far off-center to be probable counterparts.

CX1, as remarked above, is the dwarf nova discovered and studied by Kaluzny et al. (2005), whose optical position we find to be compatible with the *Chandra* position, and which we used to correct the *Chandra* coordinates. In Fig. 4 we see that the optical counterpart of CX1 has strong H $\alpha$  emission as expected, but is less blue than expected for a dwarf nova, being at the blue edge of the main sequence. Its X-ray to optical flux ratio is as expected for a cataclysmic variable, well above the line  $\log L_X = 34.0 - 0.4M_V$  that roughly separates cataclysmic variables from the magnetically active binaries below it (Fig. 7).



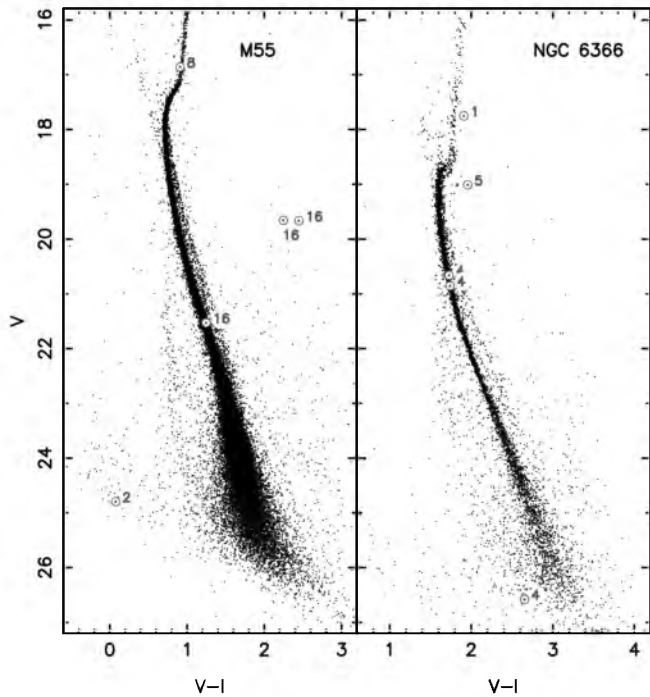


**Fig. 5.** Optical color-magnitude diagrams for M55 and NGC 6366 constructed from the Anderson et al. (2008) photometry. Candidate optical counterparts to the *Chandra* X-ray sources are indicated and numbered.

The error circle of CX2 shows a very faint blue object in the ACS/WFC observations. The source could be a cataclysmic variable, though it is below the detection limit in the FORS2 observations, so we do not know if it exhibits an excess of  $H\alpha$  emission. Compared to classified cataclysmic variables in globular clusters, the optical counterpart is significantly fainter. The probable optical counterpart of CX7 is at a position slightly below and towards the red of the subgiant branch in the colour magnitude diagram Fig. 4, and thus a sub-subgiant in the terminology introduced by Belloni et al. (1998) in their study of M67. It has no significant  $H\alpha$  emission. Its  $f_X/f_{\text{opt}}$  indicates a magnetically active binary in agreement with the classification as a sub-subgiant. The possible optical counterpart of CX8 from its position in the colour magnitude diagram appears to be an ordinary subgiant; as this star is less well centered in the astrometric confidence circle, it is quite possible that the real counterpart of CX8 is a fainter object. CX10 has two possible counterparts, the brighter one is on the binary sequence in the colour magnitude diagram, but puzzlingly has strong  $H\alpha$  absorption. Because the  $R - H\alpha$  is not affected by interstellar absorption, this offset from the main sequence cannot be explained as due to the star being a fore- or background object. This suggests it is an active binary. The *HST* observations show that the single star found in the error circle of CX16 in the FORS2 observations is in fact a blend of three stars. Two of these stars are rather red and too far from the main sequence of M55 to be a member. Their red colours suggest they are background objects. The third star lies on the cluster main-sequence in  $V - I$ , and could indicate that the star is an active binary. Because the star is blended in the FORS2 observations, it is unclear to which object the  $H\alpha$  absorption can be attributed.

For the sources outside the half-mass radius of M55, CX19 has two candidate counterparts, one on the subgiant branch, the other on the main-sequence. Neither counterpart displays a sig-

nificant emission or absorption of  $H\alpha$  flux. CX20 on the other hand has very strong  $H\alpha$  emission and is very blue in  $B - R$ . With a X-ray luminosity of  $L_X = 3.3 \times 10^{31} \text{ erg s}^{-1}$  it is very similar to CX1 and possibly a cataclysmic variable. The counterpart to CX21 is on the main-sequence and could be an active binary. However, the  $f_X/f_{\text{opt}}$  ratio of this source places it in the region that is primarily populated by CVs, the X-ray source could be a cataclysmic variable. We will return to this source in Section 5.2. CX23 shows similarities with CX16 in the sense that it is very red and has a large excess of  $H\alpha$  emission. It is likely a background object. The optical counterpart to CX24 is slightly blue but shows no  $H\alpha$  emission or absorption compared to that of the cluster stars. It is the brightest X-ray source in our sample, and it has an  $f_X/f_{\text{opt}}$  ratio that would be indicative of a cataclysmic variable. However, the absence of  $H\alpha$  suggests it belongs to the Galactic field. The optical counterpart to CX29 may be yet another sub-subgiant; it is located below the subgiant branch and has a X-ray luminosity comparable to that of CX7 in M55 and CX5 in NGC 6366. We do note that the source lies at the edge of the error circle.

#### 4.2. NGC 6366

Turning now to NGC6366, we consider four possibilities for the extended emission of source CX1b; a planetary nebula, a supernova remnant, a group or cluster of galaxies and a nova remnant. Planetary nebulae and supernovae tend to have strong  $H\alpha$  emission. The apparent absence of such emission in our  $H\alpha$  images of CX1 (Fig. 2) argues against these two possibilities. A second argument against a planetary nebula is that the X-ray spectra of planetary nebula observed with *Chandra* are rather soft, limited to energies below 1.5 keV (e.g. BD+30°3639, Kastner et al. 2000; NGC 7027, Kastner et al. 2001; NGC 6543, Chu et al. 2001), whereas 50% of the photons of CX1b is above 2 keV (Fig. 2). A second argument against a supernova remnant is that it is an unlikely object to be found in a globular cluster, or as a foreground object at a Galactic latitude of  $16^\circ$ .

The clusters of galaxies studied by Kaastra et al. (2004) and Piffaretti et al. (2005) have typical X-ray diameters of order 1 Mpc and X-ray luminosities in excess of  $10^{43} \text{ erg s}^{-1}$ . Both the flux and diameter of CX1b imply a distance of more than a Gpc if this source is a typical cluster. The intra-cluster gas in such bright clusters strongly dominates the total flux, and so the superposition of CX1a and CX1b would be accidental if CX1b is a galaxy cluster. Groups of galaxies have a smaller extent and lower X-ray luminosity, against which an individual galaxy can stand out (e.g. Nakazawa et al. 2007). However, even our deepest  $B$  and  $R$ -band images show no obvious galaxies near the position of CX1, and this excludes a group or cluster of galaxies out to several hundred Mpc.

Finally, a nova outburst may give rise to extended X-ray emission, as illustrated by the case of GK Per (Nova Persei 1901) which was detected as an extended source with *Chandra*, surrounding the point source of the cataclysmic variable GK Per itself (Balman, 2005). Both in size and in luminosity CX1 is a plausible old nova at the distance of NGC 6366, but the spectrum of the extended source CX1b is rather harder than the soft extended source surrounding GK Per. The amount of matter in a nova remnant is much less than in a planetary nebula, perhaps compatible with the absence of extended  $H\alpha$  emission; indeed, Slavin et al. (1995) argue that the faint emission around GK Per in the  $H\alpha$  filter is due largely to  $\text{N II}$  emission.

For the moment, we consider an old nova to be the more likely explanation for the X-ray source CX1 in NGC 6366.

Novae are known in globular clusters; T Sco (1860) in M80, V1148 Sgr (1943) in NGC 6553 and Nova 1938 in M14 (Sawyer, 1938; Mayall, 1949; Sawyer Hogg & Wehlau, 1964). The nova hypothesis explains the position of CX1 near the cluster center, and the superposition of CX1a on CX1b. It remains to be shown, however, that the X-ray spectrum of an old nova can be as hard as that of CX1b.

The two bright possible optical counterparts of CX4 are both ordinary main sequence stars according to the colour magnitude diagram; the  $f_X/f_{opt}$  suggests a magnetically active binary, in which case the companion does not contribute significantly to the optical fluxes. However, CX4 is a hard X-ray source which may be hard to reconcile with a magnetically active binary. It may be that the source is not related to the globular cluster and is associated with the faint optical counterpart seen in the ACS/WFC observations. The optical counterpart of CX5 is yet another sub-subgiant as CX7 in M55. For NGC 6366 CX8 coincides with the bright star BD -04°4280. With  $V = 10.7$ , it is saturated in our FORS2 observations (see Fig. 6) and hence not present in Fig. 4 and Table 5. At this brightness it is at least 8 mag brighter than the cluster turn-off and hence highly unlikely to be a member of NGC 6366. Finally CX14 has a candidate counterpart that is blue in  $B-R$  with respect to the cluster main-sequence but has no  $H\alpha$  emission or absorption. The absence of  $H\alpha$  emission suggests it belongs to the Galactic field.

## 5. Discussion

### 5.1. Comparison with earlier observations

Both M55 and NGC 6366 have been observed with *ROSAT*, and *XMM* also observed M55.

#### 5.1.1. M55

In Fig. 8 we compare the countrates of sources in M55 observed with *Chandra* (from Table 2) with those observed with *XMM* EPIC (from Table 2 of Webb et al. 2006). All *XMM* sources within the field-of-view of *Chandra* have been detected; the *XMM* sources are the sources with the highest countrates in *Chandra*, plus CX29 (*XMM*45). Comparison of the *Chandra* and *XMM* source positions shows that the error estimates by Webb et al. for the *XMM* source positions are overestimated by about a factor 2. As expected, the *XMM* countrate for most sources is  $\sim 4$  times higher than the *Chandra* countrate: for example, a 2 keV bremsstrahlung spectrum absorbed by the column towards M55, with  $0.001 \text{ cts s}^{-1}$  in *Chandra* ACIS-S will produce about  $0.0026 \text{ cts s}^{-1}$  on the PN and  $0.00075 \text{ cts s}^{-1}$  on each of the two MOS detectors, for a total of  $0.0041 \text{ cts s}^{-1}$  in *XMM*<sup>3</sup>.

Remarkably, all three sources with the lowest *XMM* count rates were brighter during the *Chandra* observation. One of these is the cataclysmic variable CV1, our source CX1. Webb et al. (2006) state that this source was three times fainter, in the 0.5–10 keV band, during the *XMM* observation than during earlier *ROSAT* observations. Since the *ROSAT* measurements are limited to the 0.2–2.5 keV band, we prefer to make the comparison of the luminosities in this energy range. The hardness ratio of CX1 as measured with *Chandra* (see Fig. 3) is that of a bremsstrahlung spectrum with temperature  $kT_b \simeq 2 \text{ keV}$ .

<sup>3</sup> We estimate this with the PIMMS tool at <http://heasarc.gsfc.nasa.gov/Tools/w3pimms.html>; we have multiplied the countrates within a  $15''$  extraction radius as given by PIMMS with 1.47 to estimate the total countrates

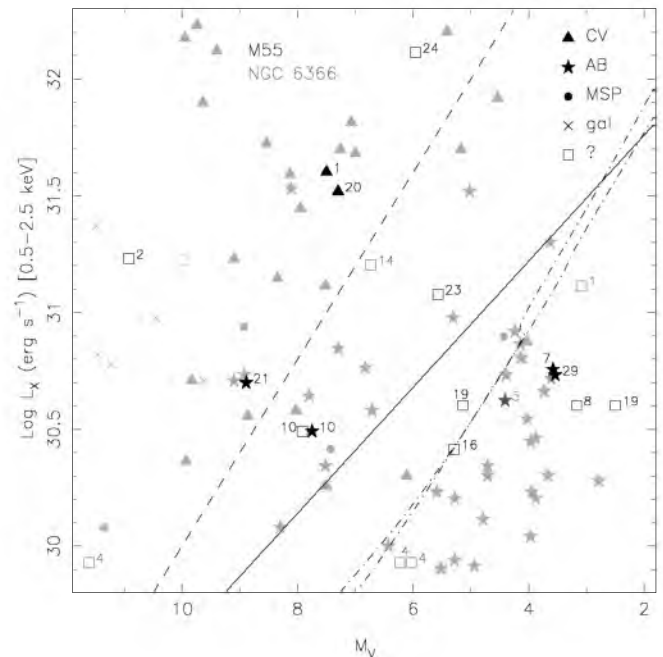


**Fig. 7.** The 0.5–2.5 keV X-ray luminosity  $L_X$  against the absolute  $V$ -band magnitudes. The  $V$ -band magnitudes are estimated by  $V = (B + R)/2$  to allow a comparison to X-ray sources with optical counterparts detected in other globular clusters. The X-ray sources are classified into the different classes as indicated. Besides the *Chandra* X-ray sources discovered in M55 and NGC 6366 (which are numbered) we also have included classified X-ray sources from 47 Tuc, NGC 6752, NGC 288, NGC 6397,  $\omega$  Cen, M22 and M4. The diagonal dashed line of constant X-ray to optical luminosity ratio ( $\log L_X = 34.0 - 0.4M_V$ ) roughly separates CVs from ABs (after Bassa et al. 2004). The solid diagonal line ( $\log L_X = 32.3 - 0.27M_V$ ) is after Verbunt et al. (2007). The two dashed-dotted lines are computed from 11.2 Gyr isochrones at  $z = 0.001$  and  $z = 0.019$  from Girardi et al. (2000), assuming  $L_X \simeq 0.001L_{bol}$ .

Assuming this spectrum, the distance and absorption of M55 as above, and the countrates given in Table 3 of Verbunt (2001); cf. Johnston et al. (1996) and in Table 2 of Webb et al. (2006), we obtain 0.5–2.5 keV luminosities, in units of  $10^{31} \text{ erg s}^{-1}$ , of  $6.0 \pm 1.5$  for both the *ROSAT* PSPC observation (March 1991) and the *ROSAT* HRI observation (September 1997), and of  $0.44 \pm 0.09$  for the *XMM* observation (October 2001); our *Chandra* observation (May 2004, Table 1) gives  $4.1 \pm 0.4$ . Thus, the X-ray flux was an order of magnitude lower during the *XMM* observation than during the *ROSAT* and *Chandra* observations. Webb et al. (2006) assume that the X-ray flux is higher during an optical/ultraviolet dwarf nova outburst, and conclude that CV1 was in outburst during both *ROSAT* observations. However, most dwarf novae have lower X-ray fluxes during outburst than in quiescence (Wheatley et al. 1996; Verbunt et al. 1999 and the discussion of Fig. 2 in Verbunt et al. 1997). We conclude that CV1 was in outburst during the *XMM* observations, and in quiescence during the *ROSAT* and *Chandra* observations, in good agreement with the observations by Kaluzny et al. (2005) that CV1 spends most of the time in quiescence.

We detect the optical counterpart to CV1 at  $R = 20.7$  and  $B - R = 1.34$ , where it lies only about 0.3 mag blue-wards of the cluster main-sequence. With  $R - H\alpha = 0.58$ , it exhibits a large excess of  $H\alpha$  emission, reminiscent of cataclysmic variables. At

**Table 5.** Candidate optical counterparts to the *Chandra* X-ray sources. The positional offsets are given relative to the *Chandra* values in Tables 2 and 3. The X-ray luminosity is in the 0.5–2.5 keV energy range. The first optical counterpart to CX16 is a blend of the three other stars.

CX	$\Delta\alpha$	$\Delta\delta$	$R$	$B - R$	$R - H\alpha$	$V$	$V - I$	$L_X$ ( $\text{erg s}^{-1} \text{cm}^{-2}$ )
M55								
1	0′:00	−0′:00	20.69(1)	1.36(2)	0.58(2)			$4.0 \times 10^{31}$
2	0′:18	−0′:03				24.80(2)	0.1(3)	$1.7 \times 10^{31}$
7	−0′:06	−0′:11	16.75(1)	1.40(1)	0.03(1)			$5.7 \times 10^{30}$
8	0′:28	0′:12	16.45(1)	1.19(1)	−0.00(1)	16.86(1)	0.91(1)	$4.0 \times 10^{30}$
10	−0′:04	0′:03	20.51(4)	2.23(6)	−0.36(8)			$3.1 \times 10^{30}$
10	0′:53	0′:28	20.90(2)	1.79(3)	0.01(3)			$3.1 \times 10^{30}$
16	0′:14	0′:09	17.82(1)	2.68(3)	0.31(1)			$2.6 \times 10^{30}$
16	0′:24	0′:04				19.66(2)	2.25(2)	$2.6 \times 10^{30}$
16	0′:24	0′:15				19.67(2)	2.50(2)	$2.6 \times 10^{30}$
16	−0′:13	−0′:00				21.53(1)	1.25(1)	$2.6 \times 10^{30}$
19	0′:25	0′:47	15.78(1)	1.18(1)	0.07(1)			$4.0 \times 10^{30}$
19	0′:35	−0′:52	18.45(1)	1.01(2)	−0.09(2)			$4.0 \times 10^{30}$
20	0′:20	0′:09	21.25(6)	−0.16(6)	0.51(7)			$3.3 \times 10^{31}$
21	−0′:09	−0′:48	21.70(1)	2.12(3)	−0.00(2)			$5.0 \times 10^{30}$
23	0′:13	0′:06	18.13(2)	2.63(3)	0.50(4)			$1.2 \times 10^{31}$
24	0′:04	−0′:26	19.41(1)	0.73(1)	0.03(1)			$1.3 \times 10^{32}$
29	0′:61	−0′:19	16.68(1)	1.46(1)	0.04(1)			$5.4 \times 10^{30}$
NGC 6366								
1	0′:21	0′:24	16.73(1)	2.66(1)	0.03(1)	17.75(1)	1.91(1)	$1.3 \times 10^{31}$
4	0′:29	0′:34	19.84(1)	2.32(2)	−0.03(2)	20.66(1)	1.73(1)	$8.5 \times 10^{29}$
4	−0′:08	−0′:23	20.02(1)	2.36(2)	0.00(2)	20.85(1)	1.74(1)	$8.5 \times 10^{29}$
4	0′:18	−0′:27				26.6(3)	2.6(3)	$8.5 \times 10^{29}$
5	−0′:05	0′:07	18.11(1)	2.56(2)	0.06(1)	19.01(1)	1.96(1)	$4.2 \times 10^{30}$
14	0′:22	0′:68	20.78(1)	1.83(1)	0.04(2)			$1.6 \times 10^{31}$

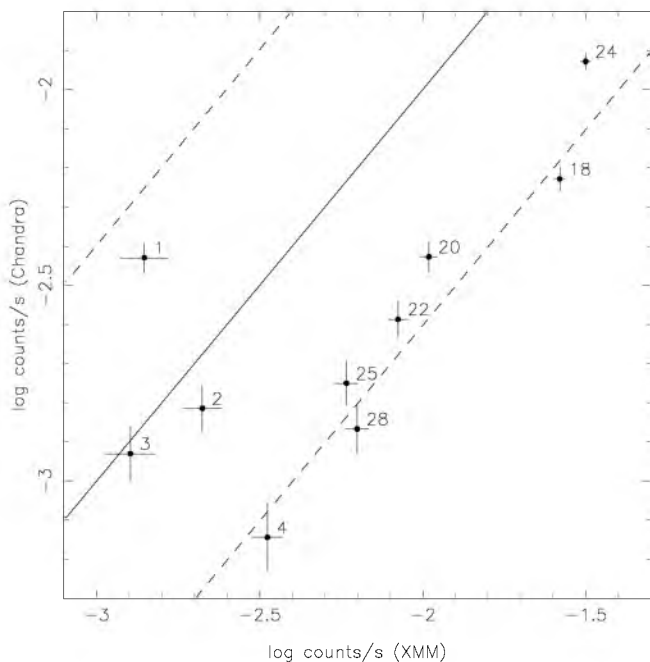


**Fig. 8.** Detected count rate in the 0.5–6.0 keV energy band ( $X_{\text{soft}} + X_{\text{hard}}$ , Table 2) of the *Chandra* ACIS-S observation as a function of the *XMM* EPIC (PN and both MOS detectors) count rate in the 0.5–10 keV energy band (Table 2 of Webb et al. 2006). The solid and dashed lines show equal count rates and 4 times higher/lower count rates, respectively. For most sources, the *XMM* count rate is about 4 times higher than the *Chandra* count rate, as expected for a constant source.

$B = 22.1$ , our photometry of CV1 puts it close to the quiescent level of about  $B = 22.5$  seen in the light-curve by Kaluzny et al. (2005). Furthermore, the proximity in color of the source to the cluster main-sequence was also seen by Kaluzny et al. (2005) during quiescence, where the source actually coincides with the main-sequence in  $B - V$  and  $V - I$  (see Fig. 4 of Kaluzny et al.). Hence, we conclude that CX1/CV1 was also in quiescence during our FORS2 observations.

Fig. 8 shows that CX20/XMM14 had *Chandra* and *XMM* count rates as expected for a constant luminosity between the two observations. The source was not detected with *ROSAT*; in re-analysing the *ROSAT* PSPC observation, using the method outlined in Verbunt (2001), we obtain a  $2\sigma$  upper limit to the count rate of  $0.0006 \text{ cts s}^{-1}$  (channels 50–240), which corresponds roughly to a flux at 0.5–2.5 keV of  $8.9 \times 10^{-15} \text{ erg cm}^{-2} \text{ s}^{-1}$ . Analysis of the HRI data gives an upper limit of 10 source counts, or  $8 \times 10^{-15} \text{ erg cm}^{-2} \text{ s}^{-1}$ . Within the error, these limits are compatible with the flux found with *Chandra* (Table 2) and with *XMM*. Webb et al. (2006) argue that this source has been variable by at least a factor 22 between the *ROSAT* and *XMM* observations. We find no evidence for such variation.

Kaluzny et al. (2005) discuss an interesting blue variable star, which they name M55-B1. From its variability between observing seasons, in the absence of short-term ( $\sim \text{hr}$ ) variability, they argue that it is a background quasar rather than a cataclysmic variable. This source is not detected on the *Chandra* ACIS-S3 chip, but on an adjacent chip. It is clearly detected in X-rays, with an unabsorbed flux in the 0.5–8.0 keV band of  $5.1 \times 10^{-15} \text{ erg cm}^{-2} \text{ s}^{-1}$  for absorption fixed at that of M55. A free power law fit gives a higher absorption ( $N_{\text{H}} = 7.4 \times 10^{21} \text{ cm}^{-2}$ ) and higher unabsorbed flux of  $8.8 \times 10^{-15} \text{ erg s}^{-1}$ .

### 5.1.2. NGC 6366

Only the brightest *Chandra* source was detected with *ROSAT*, at a 0.5–2.5 keV luminosity (Verbunt, 2001) compatible with that during the *Chandra* observation. *ROSAT* observed CX1a and CX1b as one source. The observed spectrum of the point source is relatively soft (see Fig. 2, and Sect. 2.3), which with the high absorption towards NGC 6366 implies a very soft intrinsic spectrum. Whereas many cataclysmic variables have hard spectra, a very soft spectrum is still compatible with identification as an old nova.

### 5.2. Ratio of optical to X-ray luminosity

Our classification of the X-ray sources for which we have an optical identification is based in part on the X-ray to optical luminosity ratio. Bassa et al. (2004) showed that a line of constant *Chandra* X-ray to optical luminosity roughly separates the cataclysmic variables from the active binaries in 47 Tuc, NGC 6752 and M4 (data from Grindlay et al. 2001; Edmonds et al. 2003; Pooley et al. 2002; Bassa et al. 2004). This separatrix corresponds to the dashed line in Fig. 7, and is given by

$$\log L_X(\text{erg s}^{-1}) [0.5\text{--}2.5 \text{ keV}] = 34.0 - 0.4M_V \quad (1)$$

Remarkably, and perhaps disconcertingly, this line is rather higher than the upper bound to the X-ray luminosities of stars and RS CVn binaries near the Sun. An upper bound is given in Verbunt et al. (2007) as

$$\log L_X(\text{erg s}^{-1}) [0.5\text{--}2.5 \text{ keV}] = 32.3 - 0.27M_V \quad (2)$$

This line is an absolute upper bound in that it lies above all *ROSAT* measurements for nearby stars (selected from Hünsch et al. 1999) and for RS CVn systems (Dempsey et al., 1993), where we multiply the 0.1–2.4 keV luminosities given by Hünsch et al. and Dempsey et al. with 0.4 to obtain the 0.5–2.5 keV luminosities. It is shown as a solid line in Fig. 7. It has been remarked already on the basis of *Einstein* 0.2–4 keV measurements that the X-ray luminosity of main-sequence stars increases with increasing stellar rotation velocity, until it saturates at

$$L_X \simeq 0.001L_{\text{bol}} \quad (3)$$

where  $L_{\text{bol}}$  is the bolometric luminosity of the star (e.g. Vilhu & Walter 1987, esp. their Fig. 6).

We show in Fig. 7 the line of  $0.001L_{\text{bol}}$  for the 11.2 Gyr isochrones calculated by Girardi et al. (2000) for metal-poor stars ( $z = 0.001$ ), appropriate for globular clusters, and for stars of solar abundance ( $z = 0.019$ ), appropriate for stars in the solar neighbourhood. These lines differ little, and give a more conservative upper bound to the maximum 0.5–2.5 keV luminosity of stars near the Sun.

The region between the separatrix Eq. 1 on the one hand and the upper bounds given by Eq. 2 or Eq. 3 contains a dozen optical counterparts of X-ray sources in globular clusters that have been classified as magnetically active binaries. If this classification is correct, we must accept that such binaries can have rather higher X-ray luminosities in globular clusters than in the solar neighbourhood. Since the bolometric luminosity as a function of  $M_V$  is similar for low and solar metallicities, this would imply that the saturation of X-rays occurs at higher  $L_X/L_{\text{bol}}$  in globular clusters. Alternatively, we may wish to reconsider the classification of these sources. If we want to classify them as cataclysmic variables, we must accept that globular clusters host cataclysmic

**Table 6.** Values for central density  $\rho_0$ , core radius  $r_c$ , distance  $d$ , and absolute visual magnitude  $M_V$ , taken from Harris (1996, version Feb 2003), and for M4 from Richer et al. (1997). Collision number  $\Gamma$  and mass within the half-mass radius  $M_h$  are scaled on the values for M4.

cluster	$\log \rho_0$ ( $L_\odot \text{ pc}^{-3}$ )	$r_c$ ( $''$ )	$d$ (kpc)	$M_V$	$\Gamma$	$M_h$
M4	4.01	49.8	1.73	-6.9	$\equiv 1.00$	$\equiv 1.00$
NGC 6397	5.68	3.0	2.3	-6.6	2.05	0.78
47 Tuc	4.81	24.0	4.5	-9.4	24.91	10.19
NGC 288	1.80	85.2	8.8	-6.7	0.04	0.86
M55	2.15	169.8	5.3	-7.6	0.18	1.82
NGC 6366	2.42	109.8	3.6	-5.8	0.09	0.35

variables that are not blue with respect to the main sequence, even in the *B*-band filter. These systems clearly warrant further study. We note that CV1 in M55 does lie on the main-sequence in *B - V* in quiescence (Kaluzny et al. 2005, see Sect. 5.1.1).

### 5.3. Origin of the X-ray sources

To compare the numbers of X-ray sources in globular clusters, Pooley et al. (2003) chose a luminosity limit of  $L_X > 4 \times 10^{30} \text{ erg s}^{-1}$  [0.5–6.0 keV], which is detectable in almost all the clusters they investigated. We have detected 16 sources above this limit within the half-mass radius of M55, with an expected number of 8–9 unrelated sources; and 5 within the half-mass radius of NGC 6366, with an expected number of 4 unrelated sources. As already argued above, from these numbers alone we cannot exclude that all detected sources are unrelated. The situation changes if we take into account our optical identifications (Section 4), which indicate that at least three sources (CX1, CX7, CX10) are highly probable members of M55, and that two sources (CX4, CX5) are highly probable members of NGC 6366. We have also argued that the point source plus extended source is an old nova in NGC 6366.

In Table 6 we compare the collision numbers  $\Gamma \equiv \rho_0^{1.5} r_c^2$  and the masses within the half-mass radii  $M_h$  (as measured with the absolute magnitude assuming a fixed mass-to-light ratio) for several well-observed clusters; where we scale both  $\Gamma$  and  $M_h$  on the globular cluster M4.

Pooley et al. (2003) report  $41 \pm 2$  sources above the luminosity limit in the core of 47 Tuc. If the number of X-ray sources would scale with the collision number, we would predict 0.3 sources in M55, and 0.15 in NGC 6366. The number of detected very probable member X-ray sources is significantly higher in both clusters. If the number of X-ray sources would scale with the mass, we would predict about 7 sources in M55, and 3 to 4 in NGC 6366. The number of detected member X-ray sources is remarkably close to this.

To study the origin of X-ray sources in globular clusters in further detail, Pooley & Hut (2006) investigate the hypothesis that the number of sources scales with the collision number and mass as

$$N = a\Gamma + bM \quad (4)$$

and show that the dependence on mass is significantly present in the observations. To overcome the small-number statistics of clusters with small source numbers, they combine the numbers of such clusters before fitting them to Eq. 4.

In a recent paper, Verbunt et al. (2007) suggest a more general way of fitting the observed numbers to Eq. 4. Briefly, they

determine for each cluster the most probable combination of numbers  $N_c$  of member and  $N_b$  of unrelated sources that gives the observed number of sources within the half-mass radius  $N_h$ , based on the expected number of cluster sources  $\mu_c$  according to the model of Eq. 4, and on the expected number of unrelated sources  $\mu_b$ . In doing so they assume that the probability of finding  $N$  sources when  $\mu$  are expected is given by the Poisson function

$$P(N, \mu) = \frac{\mu^N}{N!} e^{-\mu} \quad (5)$$

The fitting procedure consists of varying  $a$  and  $b$  to maximize

$$P = \prod_j [P(N_c, \mu_c) P(N_b, \mu_b)]_j \quad (6)$$

where  $j$  indexes the clusters.

The values for  $N_h$  and  $\mu_c$  that we use are taken from Pooley et al. (2003). We ignore the clusters for which only a lower limit to  $N_h$  is known. We add three clusters: NGC 288, M55 and NGC 6366; the values we use are 11/8.0, 16/8.3 and 5/4.0 for  $N_h/\mu_c$  for these three clusters, respectively. The best solution is found for  $a = 1.3\Gamma_{M4}$  and  $b = 0.6M_{M4}$ . The contours of the acceptable solutions are given in Fig. 9, and it is seen that  $b = 0$  is acceptable at about the  $2\sigma$  level. Thus, from the observed numbers alone, we have no firm evidence for a dependence on mass.

We repeated the fitting procedure, but excluding solutions for which  $N_c$  is less than the minimum number of highly probable cluster members. For these fits we assume that 2 sources are certain members of NGC 288, 3 of M55 and 2 of NGC 6366. As expected, these constraints force the solutions to a stronger dependence on mass: the best solution is found for  $a = 1.2\Gamma_{M4}$  and  $b = 1.1M_{M4}$ . As seen in Fig. 9, the dependence on mass is now significant.

The best values of  $a$  and  $b$  are relatively stable against small variations in the numbers  $\mu_c$  and  $N_h$  for individual clusters, as comparison with the results of Verbunt et al. (2007) confirm. The probability of the best solution does vary with small variations in  $\mu_c$  and  $N_h$  for individual clusters. For example, increasing the minimum of cluster member X-ray sources in NGC 6366 from 2 to 3 does not change the best values for  $a$  and  $b$ , but decreases the probability of the best solution for NGC 6366, for which the best model predicts  $\mu_c = 0.4$ , and thus also slightly decreases the overall probability.

The cluster which is responsible for the lowest probability is NGC 6397, which houses 12 sources, of which our best model assigns  $N_c = 11$  to be cluster members, even though it expects only  $\mu_c = 3.6$ . The remarkably large number of sources in this cluster has been remarked upon before, and various explanations have been offered. In our model, however, whereas still the worst fit cluster, it is not altogether unacceptable. The main difference between this result and the strong deviation for NGC 6397 as found by e.g. Pooley et al. (2003) appears to be due to a different definition of  $\Gamma$ . Pooley et al. (2003) integrate a King model to estimate  $\Gamma$ , whereas we compute it as  $\Gamma = \rho_0^{-1.5} r_c^2$ . Our probabilities do not take into account the uncertainties in  $\Gamma$  and  $M_h$ , nor the observed number  $N_h$  which through its dependence of the flux limit is affected by the assumed distance to the cluster. Clearly these uncertainties warrant further investigation.

An important result illustrated by Fig. 9 is that the masses of the clusters may *not* be taken as proxies for their collision numbers. Even though there is some correlation between mass and collision number, the spread in collision number at given mass, and in mass at given collision number, is very large. Indeed

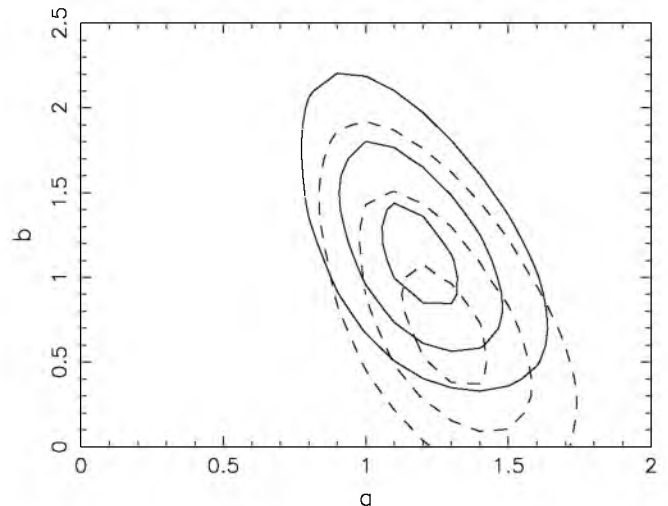


**Fig. 9.** Probability contours around the best solutions for a fit of the observed number of sources within the half-mass radii of 12 globular clusters to Eq. 4 where we allow zero cluster members in some clusters (dashed contours), and where we impose lower limits to the number of cluster members of 2 for NGC 288, 3 for M55 and 2 for NGC 6366 (solid contours). We assume that  $-2(P - P_{\text{bf}})$ , with the probability  $P$  given by Eq. 6 and  $P_{\text{bf}}$  indicating the best fit probability, follows a  $\chi^2$  distribution, and show  $\Delta\chi^2 = 1, 4$  and  $9$ . The imposition of minimum numbers of cluster member X-ray sources strongly increases the significance of the mass dependence in Eq. 4.

our fits show that the number of X-ray sources within a cluster is very badly predicted by the mass alone, as illustrated by the highly significant offset of the best solution from the  $a = 0$  line.

*Acknowledgements.* We thank Jacco Vink for drawing our attention to the extended emission of old novae. We thank Ata Sarajedini and Jay Anderson for providing us with the data for Fig. 5 in advance of publication. W.H.G.L. is grateful for generous support from NASA. C.G.B. acknowledges support from NWO.

## References

- Aldcroft, T. L., Karovska, M., Cresitello-Dittmar, M. L., Cameron, R. A., & Markevitch, M. L. 2000, in Proc. SPIE Vol. 4012, p. 650-657, X-Ray Optics, Instruments, and Missions III, Joachim E. Truemper; Bernd Aschenbach; Eds., ed. J. E. Truemper & B. Aschenbach, 650-657
- Anderson, J., Sarajedini, A., Bedin, L. R., et al. 2008, AJ, 135, 2055
- Balman, S. 2005, ApJ, 627, 933
- Bassa, C., Pooley, D., Homer, L., et al. 2004, ApJ, 609, 755
- Belloni, T., Verbunt, F., & Mathieu, R. 1998, A&A, 339, 431
- Broos, P. S., Townsley, L. K., Getman, K., & Bauer, F. E. 2002, ACIS Extract, An ACIS Point Source Extraction Package (University Park, Pennsylvania State Univ.)
- Cash, W. 1979, ApJ, 228, 939
- Chu, Y.-H., Guerrero, M. A., Gruendl, R. A., Williams, R. M., & Kaler, J. B. 2001, ApJ, 553, L69
- Davies, M. 1997, MNRAS, 288, 117
- Dempsey, R., Linsky, J., Fleming, T., & Schmitt, J. 1993, ApJS, 86, 599
- Edmonds, P. D., Gilliland, R. L., Heinke, C. O., & Grindlay, J. E. 2003, ApJ, 596, 1177
- Freeman, P., Doe, S., & Siemiginowska, A. 2001, in Proc. SPIE Vol. 4477, p. 76-87, Astronomical Data Analysis, Jean-Luc Starck; Fionn D. Murtagh; Eds., ed. J.-L. Starck & F. D. Murtagh, 76-87
- Gendre, B., Barret, D., & Webb, N. 2003, A&A, 403, L11
- Giacconi, R., Rosati, P., Tozzi, P., et al. 2001, ApJ, 551, 624
- Girardi, L., Bressan, A., Bertelli, G., & Chiosi, C. 2000, A&AS, 141, 371
- Grindlay, J., Heinke, C., Edmonds, P., & Murray, S. 2001, Science, 292, 2290
- Harris, W. 1996, AJ, 112, 1487
- Heinke, C. O., Grindlay, J. E., Edmonds, P. D., et al. 2005, ApJ, 625, 796

- Heinke, C. O., Grindlay, J. E., Lugger, P. M., et al. 2003, *ApJ*, 598, 501
- Heinke, C. O., Wijnands, R., Cohn, H. N., et al. 2006, *ApJ*, 651, 1098
- Hünsch, M., Schmitt, J., Sterzik, M., & Voges, W. 1999, *A&AS*, 135, 319
- Hurley, J. R., Aarseth, S. J., & Shara, M. M. 2007, *ApJ*, 665, 707
- Ivanova, N., Heinke, C. O., Rasio, F. A., et al. 2006, *MNRAS*, 372, 1043
- Johnston, H., Verbunt, F., & Hasinger, G. 1996, *A&A*, 309, 116
- Jordán, A., Côté, P., Ferrarese, L., et al. 2004, *ApJ*, 613, 279
- Kaastra, J. S., Tamura, T., Peterson, J. R., et al. 2004, *A&A*, 413, 415
- Kaluzny, J., Pietrukowicz, P., Thompson, I. B., et al. 2005, *MNRAS*, 359, 677
- Kastner, J. H., Soker, N., Vrtiliek, S. D., & Dgani, R. 2000, *ApJ*, 545, L57
- Kastner, J. H., Vrtiliek, S. D., & Soker, N. 2001, *ApJ*, 550, L189
- Kong, A. K. H., Bassa, C., Pooley, D., et al. 2006, *ApJ*, 647, 1065
- Kundu, A., Maccarone, T. J., & Zepf, S. E. 2002, *ApJ*, 574, L5
- Mayall, M. W. 1949, *AJ*, 54, 191
- Nakazawa, K., Makishima, K., & Fukazawa, Y. 2007, *PASJ*, 59, 167
- Piffaretti, R., Jetzer, P., Kaastra, J. S., & Tamura, T. 2005, *A&A*, 433, 101
- Pooley, D. & Hut, P. 2006, *ApJ*, 646, L143
- Pooley, D., Lewin, W., Homer, L., et al. 2002, *ApJ*, 569, 405
- Pooley, D., Lewin, W. H. G., Anderson, S. F., et al. 2003, *ApJ*, 591, L131
- Predehl, P. & Schmitt, J. 1995, *A&A*, 293, 889
- Richer, H. B., Fahlman, G. G., Ibata, R. A., et al. 1997, *ApJ*, 484, 741
- Röser, S. & Bastian, U. 1988, *A&AS*, 74, 449
- Sawyer, H. B. 1938, *JRASC*, 32, 69
- Sawyer Hogg, H. & Wehlau, A. 1964, *JRASC*, 58, 163
- Slavin, A. J., O'Brien, T. J., & Dunlop, J. S. 1995, *MNRAS*, 276, 353
- Stetson, P. B. 1987, *PASP*, 99, 191
- Stetson, P. B. 2000, *PASP*, 112, 925
- Verbunt, F. 2001, *A&A*, 368, 137
- Verbunt, F. 2003, in *New horizons in globular cluster astronomy*, ed. S. D. G. Piotto, G. Meylan & M. Riello (ASP Conf. Ser. Vol. 296), 245–254
- Verbunt, F., Bunk, W., Ritter, H., & Pfeffermann, E. 1997, *A&A*, 327, 602
- Verbunt, F. & Hut, P. 1987, in *The Origin and Evolution of Neutron Stars*, IAU Symposium No. 125, ed. D. Helfand & J.-H. Huang (Dordrecht: Reidel), 187
- Verbunt, F. & Lewin, W. H. G. 2006, *Globular cluster X-ray sources (Compact stellar X-ray sources)*. Edited by Walter Lewin & Michiel van der Klis. Cambridge Astrophysics Series, No. 39. Cambridge, UK: Cambridge University Press), 341–379
- Verbunt, F., Pooley, D., & Bassa, C. 2007, in *IAU Symposium*, Vol. 246, IAU Symposium, 301–310
- Verbunt, F., Wheatley, P., & Mattei, J. 1999, *A&A*, 346, 146
- Vilhu, O. & Walter, F. M. 1987, *ApJ*, 321, 958
- Webb, N. A., Wheatley, P. J., & Barret, D. 2006, *A&A*, 445, 155
- Wheatley, P., Verbunt, F., Belloni, T., et al. 1996, *A&A*, 307, 137
- Zacharias, N., Urban, S. E., Zacharias, M. I., et al. 2004, *AJ*, 127, 3043

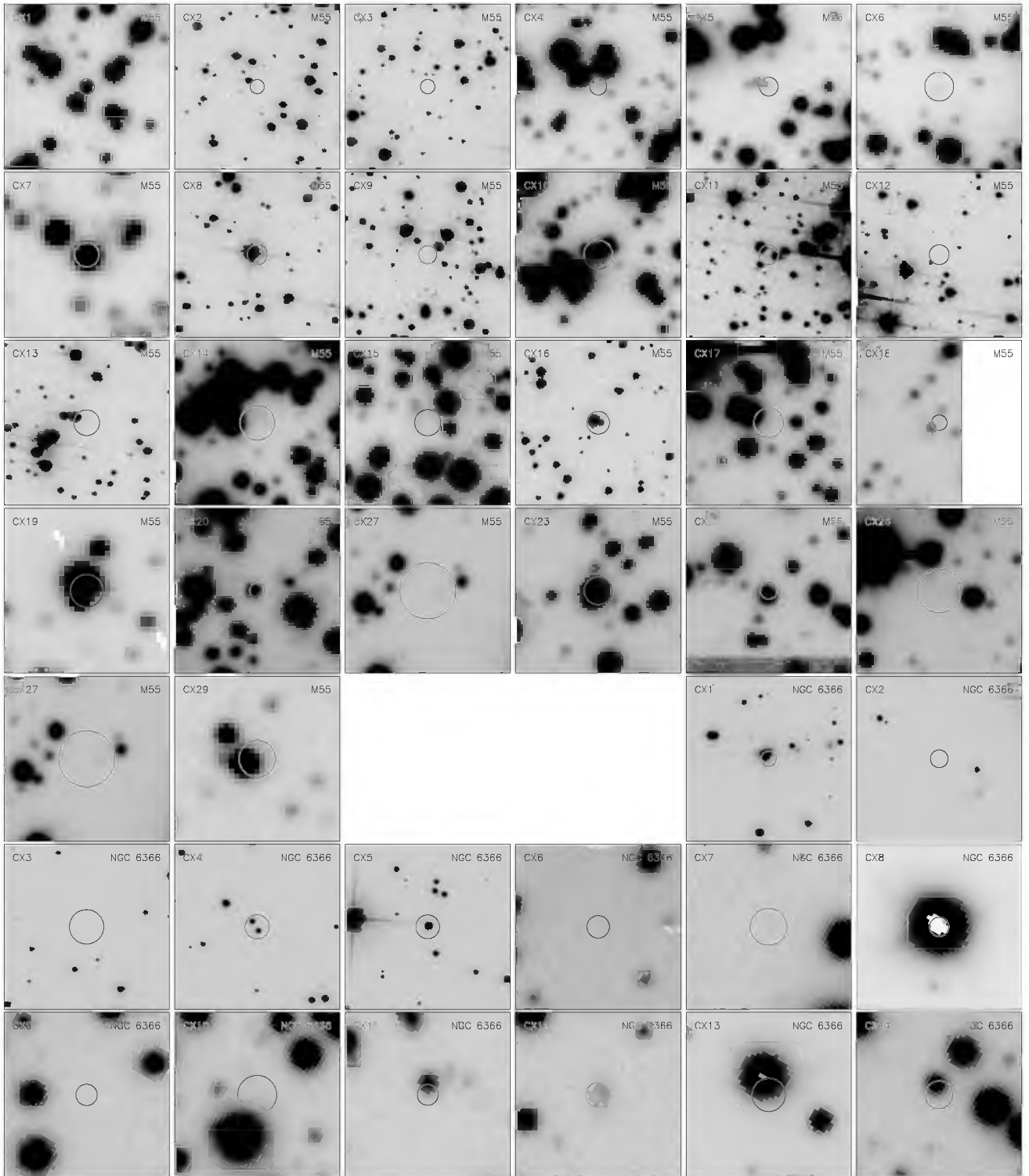


**Fig. 6.** Finding charts for all *Chandra* X-ray sources in M55 and NGC 6366 which coincide with the FORS2 or ACS/WFC field-of-view (see Fig. 1). The first 26 charts, CX1 to CX29 are for sources in M55 and are  $8'' \times 8''$  in size. Sources CX1 to CX17 are located in the cluster half-mass radius, the other sources are located outside of it. The next 14 charts are for all X-ray sources in NGC 6366 and these are  $10'' \times 10''$  in size. The first 5 are for sources inside the half-mass radius, the other 9 outside the half-mass radius. The ACS/WFC images have a 5 times better pixel scale and show the drizzled F606W observations. The finding charts for the other sources were constructed from the *R*-band FORS2 observations. The uncertainties on the X-ray source position is indicated with a 99% confidence error circle. All images have North to the top and East to the left.